UILU-ENG-97-2001

CIVIL ENGINEERING STUDIES

STRUCTURAL RESEARCH SERIES No. 614

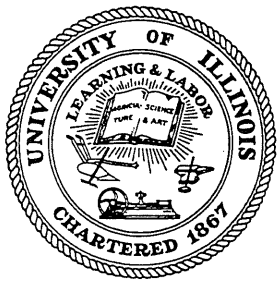

ISSN: 0069-4274

Shock Compression in Granular Media Using Discrete Finite Element Method

Jamshid Ghaboussi
and
Abdolreza Joghataie

Final Report on a Research Project
Sponsored by the
Los Alamos National Laboratory
Research Contract: LANL 6911J00149G

DEPARTMENT OF CIVIL ENGINEERING
UNIVERSITY OF ILLINOIS AT
URBANA-CHAMPAIGN
URBANA, ILLINOIS
January 1997

Shock Compression in Granular Media Using Discrete Finite Element Method

Jamshid Ghaboussi
Abdolreza Joghataie

University of Illinois at Urbana–Champaign
Urbana, Illinois 61801

Final Report on a Research Project
Sponsored by
Los Alamos National Laboratory
Contract No. LANL 6911J00149G

January 1997

Shock Compression in Granular Media Using Discrete Finite Element Method

Table of Contents

Shock Compression in Granular Media Using Discrete Finite Element Method

Jamshid Ghaboussi and Abdolreza Joghataie

Department of Civil Engineering
University of Illinois at Urbana–Champaign
Urbana, Illinois 61801

1. Introduction

This report describes the work done under a LANL contract in modeling of the shock formation and detonation in energetic materials. The methodology selected for modeling and analysis of these class problems was to use Discrete Finite Element Method (DFEM) which was originally developed by J. Ghaboussi and his co–workers for analysis of problems in geo–mechanics. In DFEM each particle of material can be modelled by a finite element mesh. The number of elements to be used in modelling of each particle will depend on a number of factors, including the desired accuracy of modeling, size of the particles and computational efficiency. The particles modeled by finite element meshes are in contact with their adjacent particle. Any contact between two particle will involve a number of individual contacts between the finite elements in the two particles. A major component of the analysis of these systems is the detection of the contacts. The deformations and the forces produced at the contacts are determined from the contact constitutive models which was developed under this contract and will be described later.

In the class of problems considered here, very large deformations are expected to develop in the granular material. The possibility of very large deformation in the particles and the contact dynamics between particles necessitated the use of the Updated Lagrangian Method (UDL). The large deformation mechanics is formulated through Lagrangian method

while, in the finite element model, the geometry of the reference configuration is frequently updated in order to keep the displacements from the reference configuration small.

In order to model the constitutive behavior of the material within the particles, the Cap model was chosen. Cap model was originally developed for modeling and analysis of geomaterials subjected to very high pressures from high explosives. With the proper choice of the material parameters, it was decided that the Cap Model can be used to represent the material behavior under shock conditions.

A computer program was developed under this contract for dynamic thermo–mechanical analysis of the particulate material using DFEM with UPL method and Cap model. This computer program was used to model and simulate an experiment.

2. Finite Element Formulation

The particles are modeled by individual finite element meshes. In this study we have used four node isoparametric elements with bilinear variation of the state variables within each element. A typical particle, its finite element mesh and a typical isoparametric element is shown in Figure 1. The nodal degrees of freedom consist of two displacements u_x and u_y, and the temperature τ. The variation of these state variables within each element are defined through shape functions N_1 through N_4.

$$u_x = N\ U_x \tag{1}$$

$$u_y = N\ U_y \tag{2}$$

$$\tau = N\ T \tag{3}$$

In this equation **N** is the matrix of shape functions and $\mathbf{U_x}$, $\mathbf{U_y}$, are the vectors of nodal displace-

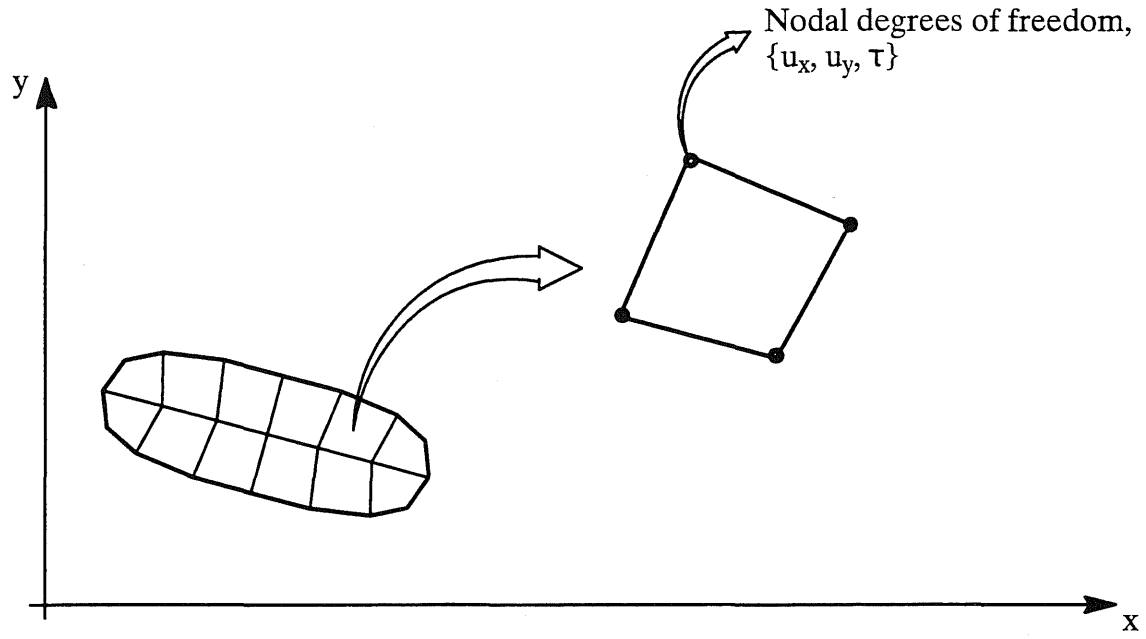

Figure 1. A typical deformable particle modeled with a finite element mesh and a typical isoparametric finite element.

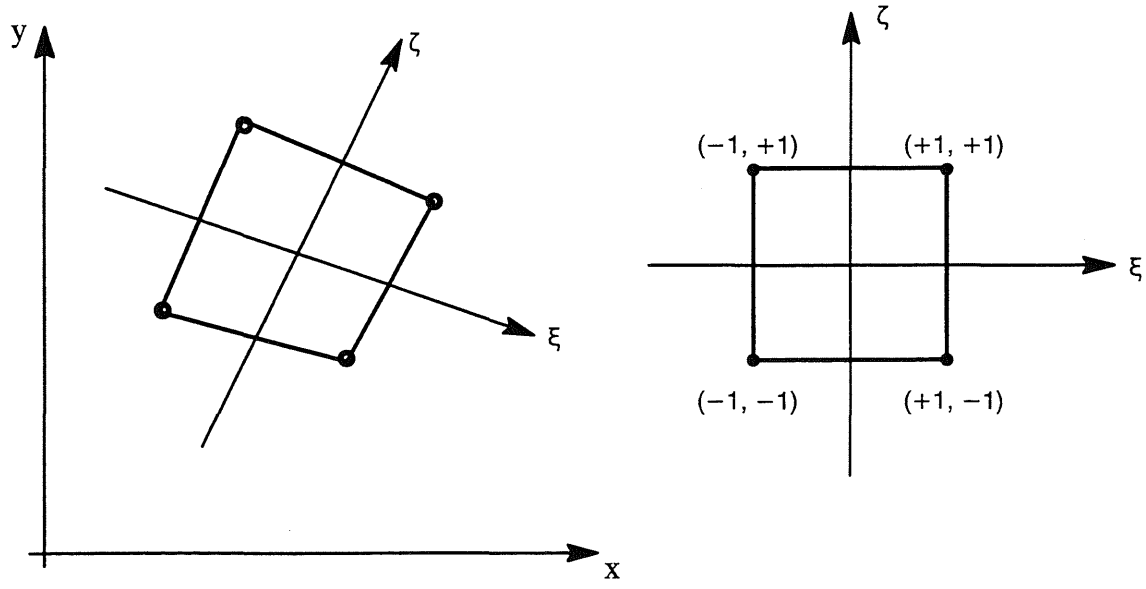

Figure 2. (a) The natural coordinate axes of the isoparametric element, (b) The parent element and the natural coordinates of the nodes

ments and **T** is the vector of nodal temperatures.

$$\boldsymbol{U_x} = \begin{Bmatrix} u_{x1} \\ u_{x2} \\ u_{x3} \\ u_{x4} \end{Bmatrix} \tag{4}$$

$$\boldsymbol{U_y} = \begin{Bmatrix} u_{y1} \\ u_{y2} \\ u_{y3} \\ u_{y4} \end{Bmatrix} \tag{5}$$

$$\boldsymbol{T} = \begin{Bmatrix} \tau_1 \\ \tau_2 \\ \tau_3 \\ \tau_4 \end{Bmatrix} \tag{6}$$

As shown in Figure 2, the parent element is defined in such a way that the nodal coordinates take on values of -1 and $+1$ in the natural coordinate system ξ and ζ. The shape functions are defined as bilinear interpolation functions in the natural coordinate system.

$$\begin{aligned} N_1 &= (1 - \xi)\ (1 - \zeta)/4 \\ N_2 &= (1 + \xi)\ (1 - \zeta)/4 \\ N_3 &= (1 + \xi)\ (1 + \zeta)/4 \\ N_4 &= (1 - \xi)\ (1 + \zeta)/4 \end{aligned} \tag{7}$$

The mapping from the natural coordinate system to the x–y coordinate system is also provided by the same shape functions.

$$x(\xi,\ \zeta) = \boldsymbol{N}\ \boldsymbol{X} \tag{8}$$

$$y(\xi,\ \zeta) = \boldsymbol{N}\ \boldsymbol{Y} \tag{9}$$

The vectors **X** and **Y** are the nodal coordinate vectors.

$$X = \begin{Bmatrix} x_1 \\ x_2 \\ x_3 \\ x_4 \end{Bmatrix} \tag{10}$$

$$Y = \begin{Bmatrix} y_1 \\ y_2 \\ y_3 \\ y_4 \end{Bmatrix} \tag{11}$$

The formulation of the stiffness matrices and load vectors, as well as the numerical integration follow the standard procedures, readily available in the relevant technical literature.

3. Coupled Discrete Finite Element Equations for Particles

The discrete finite element equations consist of two set of coupled equations: a dynamic equation of motion which describes the balance of forces and an equation describing the balance of the thermal flux and thermal energy conservation. Three sources of thermo−mechanical coupling are considered to be important in the class of problems considered in this study.

1. The thermal expansion caused by the temperature changes
2. Dependence of the material parameters on the temperature.
3. Thermal source generated by the dissipated inelastic strain energy

3.1. Updated Lagrangian Method for Dynamic Equation of Motion

The discrete dynamic equation of motion is determined from virtual work expression written at the current configuration, referring to the reference configuration.

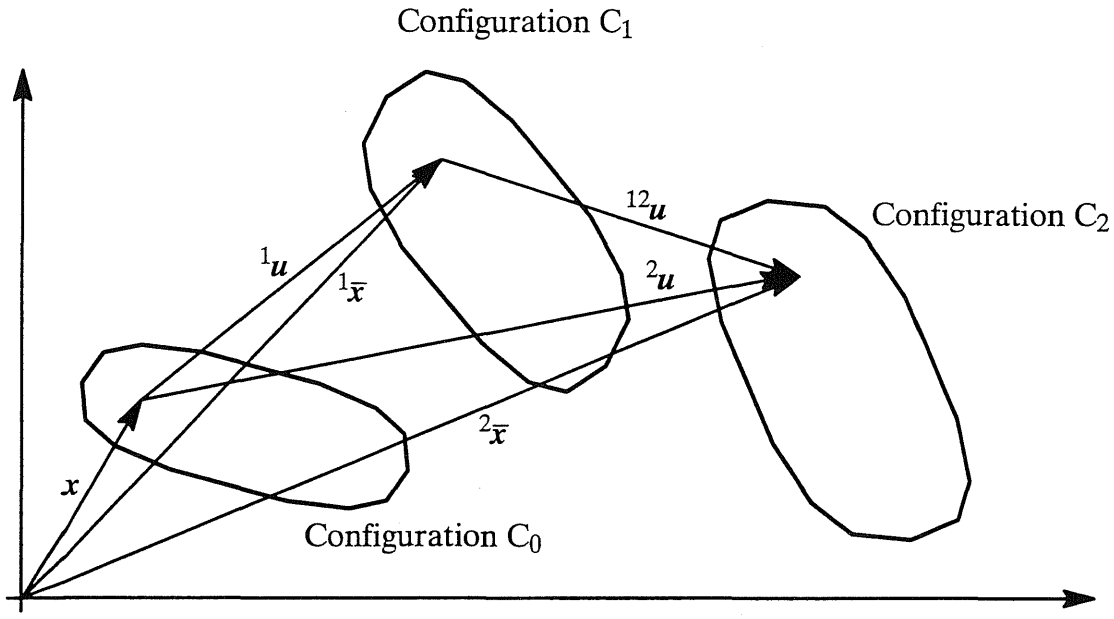

Figure 3. The definition of the initial, reference and current configurations and the associated coordinates and the displacement vectors.

$$\int_{^1V} \delta \, {}^2_1\boldsymbol{\epsilon}^T \, {}^2_1\boldsymbol{\sigma} \;\; d^1v \; + \int_{^1V} \delta \, {}^2\ddot{\boldsymbol{u}}^T \, \varrho \, {}^2\boldsymbol{u} \;\; d^1v - \int_{^1V} \delta \, {}^2\boldsymbol{u}^T \;\; {}^2\boldsymbol{f} \;\; d^1v$$

$$- \int_{^1A} \delta \, {}^2\boldsymbol{u}^T \;\; {}^2\boldsymbol{t} \;\; d^1a = 0 \qquad (12)$$

The first term is the internal virtual work (strain energy) and the last three terms represent the virtual work of the inertia forces, the virtual work of the body forces and the virtual work of the surface tractions, respectively. The virtual work expression is written for the body the current configuration C_2 with the reference configuration at C_1, as shown in Figure 3 In the UDL method used in this study, the reference configuration is not the initial configuration C_0. Throughout the motion, the reference configuration C_1 is updated frequently, so as to remain close to the current configuration C_2. In the version of the UDL method used in this study, the reference configuration is updated every time step.

The strains in the virtual work expression are the total Green strains (from C_0 to C_2), at the current configuration C_2, referring to the configuration C_1.

$$ {}^{2}_{1}\boldsymbol{\epsilon} = \frac{1}{2}({}^{2}_{1}\boldsymbol{F}^{T} \; {}^{2}_{1}\boldsymbol{F} - {}^{1}_{0}\boldsymbol{F}^{T} \; {}^{1}_{0}\boldsymbol{F}) \tag{13} $$

The deformation gradients ${}^{2}_{1}F$ and ${}^{1}_{0}F$ are defined through the following equations.

$$ {}^{2}_{1}F = [{}^{2}_{1}F_{ij}] = [\frac{\partial {}^{2}\bar{x}_i}{\partial {}^{1}\bar{x}_j}] \tag{14} $$

$$ {}^{1}_{0}F = [{}^{1}_{0}F_{ij}] = [\frac{\partial {}^{1}\bar{x}_i}{\partial x_j}] \tag{15} $$

where x_i are the material coordinates at the configuration C_0 and ${}^{1}\bar{x}_i$ and ${}^{2}\bar{x}_i$ are the spatial coordinate at C_1 and C2, respectively. The deformation gradient tensors can also be written in terms of displacements by using the identities ${}^{2}\bar{\boldsymbol{x}} = {}^{1}\bar{\boldsymbol{x}} + {}^{12}\boldsymbol{u}$ and ${}^{1}\bar{\boldsymbol{x}} = \boldsymbol{x} + {}^{1}\boldsymbol{u}$.

$$ {}^{2}_{1}F = [\delta_{ij} + \frac{\partial {}^{12}u_i}{\partial {}^{1}\bar{x}_j}] \tag{16} $$

$$ {}^{1}_{0}F = [\delta_{ij} + \frac{\partial {}^{1}u_i}{\partial x_j}] \tag{17} $$

The strain–displacement relation for the Green strain ${}^{2}_{1}\boldsymbol{\epsilon}$ is obtained by substituting the expressions for the deformation gradients from Eqs 16 and 17 in Eq 13.

$$ {}^{2}_{1}\epsilon_{ij} = \frac{1}{2}({}^{2}_{1}F^{T}_{mi} \; {}^{2}_{1}F_{mj} - {}^{1}_{0}F^{T}_{mi} \; {}^{1}_{0}F_{mj}) $$

$$ = \frac{1}{2} [(\delta_{mi} + \frac{\partial {}^{12}u_m}{\partial {}^{1}\bar{x}_i})(\delta_{mj} + \frac{\partial {}^{12}u_m}{\partial {}^{1}\bar{x}_j}) - (\delta_{mi} + \frac{\partial {}^{1}u_m}{\partial x_i})(\delta_{mj} + \frac{\partial {}^{1}u_m}{\partial x_j})] $$

$$ = \frac{1}{2} [(\frac{\partial {}^{12}u_i}{\partial {}^{1}\bar{x}_j} + \frac{\partial {}^{12}u_j}{\partial {}^{1}\bar{x}_i} + \frac{\partial {}^{12}u_m}{\partial {}^{1}\bar{x}_i}\frac{\partial {}^{12}u_m}{\partial {}^{1}\bar{x}_j}) - (\frac{\partial {}^{1}u_i}{\partial x_j} + \frac{\partial {}^{1}u_j}{\partial x_i} + \frac{\partial {}^{1}u_m}{\partial x_i}\frac{\partial {}^{1}u_m}{\partial x_j})] \tag{18} $$

For the virtual work expression, the variation of the strains are needed. The variation is taken at the configuration C_2, which do not affect the displacement ${}^1\boldsymbol{u}$ at configuration C_1. Therefore, the variation of the displacements at C_1 will vanish, $\delta {}^1\boldsymbol{u} = 0$, leading to the following expression.

$$\delta {}^2_1\epsilon_{ij} = \frac{1}{2}\left(\frac{\partial \delta {}^{12}u_i}{\partial {}^1\bar{x}_j} + \frac{\partial \delta {}^{12}u_j}{\partial {}^1\bar{x}_i} + \frac{\partial {}^{12}u_m}{\partial {}^1\bar{x}_i}\frac{\partial \delta {}^{12}u_m}{\partial {}^1\bar{x}_j} + \frac{\partial {}^{12}u_m}{\partial {}^1\bar{x}_j}\frac{\partial \delta {}^{12}u_m}{\partial {}^1\bar{x}_i}\right) \tag{19}$$

The discretization of this equation over a finite element is achieved by using the element shape functions. The resulting discrete incremental strain – displacement equation contains a linear matrix B_ℓ and a nonlinear matrix $B_{n\ell}$, given by the following equations.

$$\delta {}^2_1\boldsymbol{\epsilon} = (\boldsymbol{B}_\ell + \boldsymbol{B}_{n\ell})\,\delta {}^{12}\boldsymbol{U} \tag{20}$$

$$\boldsymbol{B}_\ell = \begin{bmatrix} \boldsymbol{N}_{,{}^1\bar{x}} & \boldsymbol{0} \\ \boldsymbol{0} & \boldsymbol{N}_{,{}^1\bar{y}} \\ \boldsymbol{N}_{,{}^1\bar{y}} & \boldsymbol{N}_{,{}^1\bar{x}} \end{bmatrix} \tag{21}$$

$$\boldsymbol{B}_{n\ell} = \boldsymbol{A}\,\boldsymbol{G} \tag{22}$$

$$\boldsymbol{A} = \begin{bmatrix} \boldsymbol{\Theta}_x^T & \boldsymbol{0} \\ \boldsymbol{0} & \boldsymbol{\Theta}_y^T \\ \boldsymbol{\Theta}_y^T & \boldsymbol{\Theta}_x^T \end{bmatrix} \tag{23}$$

$$\boldsymbol{\Theta}_x = \begin{Bmatrix} u_{x,{}^1\bar{x}} \\ u_{y,{}^1\bar{x}} \end{Bmatrix} \qquad \boldsymbol{\Theta}_y = \begin{Bmatrix} u_{x,{}^1\bar{y}} \\ u_{y,{}^1\bar{y}} \end{Bmatrix} \tag{24}$$

$$\boldsymbol{G}_x = \begin{bmatrix} \boldsymbol{N}_{,{}^1\bar{x}} & \boldsymbol{0} \\ \boldsymbol{0} & \boldsymbol{N}_{,{}^1\bar{x}} \end{bmatrix} \qquad \boldsymbol{G}_y = \begin{bmatrix} \boldsymbol{N}_{,{}^1\bar{y}} & \boldsymbol{0} \\ \boldsymbol{0} & \boldsymbol{N}_{,{}^1\bar{y}} \end{bmatrix} \tag{25}$$

$$G = \begin{bmatrix} G_x & 0 \\ 0 & G_y \end{bmatrix} \tag{26}$$

The variation of the displacements from configuration C_1 to configuration C_2, $\delta^{12}U$, is the same as the variation of the total displacements at the configuration C_2, $\delta^2 U$.

$$\delta^{12}U = \delta^2 U = \begin{Bmatrix} \delta^2 U_x \\ \delta^2 U_y \end{Bmatrix} = \begin{Bmatrix} \begin{Bmatrix} \delta^2 u_{x1} \\ \delta^2 u_{x2} \\ \delta^2 u_{x3} \\ \delta^2 u_{x4} \end{Bmatrix} \\ \begin{Bmatrix} \delta^2 u_{y1} \\ \delta^2 u_{y2} \\ \delta^2 u_{y3} \\ \delta^2 u_{y4} \end{Bmatrix} \end{Bmatrix} \tag{27}$$

The stresses ${}^2_1\sigma$ in the virtual work expression of Eq. 12 are the symmetric Piola–Kirchhoff stresses at Configuration C_2 referring to configuration C_1. However, the total stress–strain relation do not exist for the types of inelastic materials considered in this study. For these materials only the rate form of the stress–strain relations do exist. Therefore, the total form of the virtual work expression in Eq. 12 can not be used directly. First, the expression for the rate of virtual work must be determined before it can be used in derivation of the finite element equations. Before determining the rate form of the virtual work expression, we need to first discretize it by introducing the following discrete forms of the total displacements and accelerations.

Substitution of Eqs. 20, 28 and 29 into Eq. 12 lead to the following discretized form of the virtual work expression.

This equation results in a dynamic equation of motion.

$$ {}^2u = \begin{Bmatrix} {}^2u_x \\ {}^2u_y \end{Bmatrix} = \begin{bmatrix} N & 0 \\ 0 & N \end{bmatrix} \begin{Bmatrix} {}^2U_x \\ {}^2U_y \end{Bmatrix} = \hat{N}\, {}^2U \tag{28} $$

$$ {}^2\ddot{u} = \begin{Bmatrix} {}^2\ddot{u}_x \\ {}^2\ddot{u}_y \end{Bmatrix} = \begin{bmatrix} N & 0 \\ 0 & N \end{bmatrix} \begin{Bmatrix} {}^2\ddot{U}_x \\ {}^2\ddot{U}_y \end{Bmatrix} = \hat{N}\, {}^2\ddot{U} \tag{29} $$

$$ \hat{N} = \begin{bmatrix} N & 0 \\ 0 & N \end{bmatrix} \tag{30} $$

$$ \delta {}^2U^T \{ \sum \int_{{}^1V} (B_\ell + B_{n\ell})^T \, {}^2_1\sigma \; d^1v + [\sum \int_{{}^1V} \varrho \, \hat{N}^T \hat{N} \, d^1v \,] \, {}^2\ddot{U} $$

$$ - \sum \int_{{}^1V} \hat{N}^T \, {}^2f \; d^1v \; - \sum \int_{{}^1A} \hat{N}^T \, {}^2t \; d^1a \; \} = 0 \tag{31} $$

$$ M \; {}^2\ddot{U}_t + I_t - P_t = 0 \tag{32} $$

$$ M = \sum \int_{{}^1V} \varrho \, \hat{N}^T \hat{N} \, d^1v \tag{33} $$

$$ I_t = \sum \int_{{}^1V} (B_\ell + B_{n\ell})^T \, {}^2_1\sigma \; d^1v \tag{34} $$

$$ P_t = \sum \int_{{}^1V} \hat{N}^T \, {}^2f \; d^1v \; + \sum \int_{{}^1A} \hat{N}^T \, {}^2t \; d^1a \tag{35} $$

The equation of motion is satisfied at time t and the three terms represent: the inertia force with the consistent mass matrix **M**; the internal force vector **I** and the force vector **P**. The force vector represents both the body forces and the surface tractions. For the class of problems considered here the body force is the affect of the gravity and the surface tractions are mainly the contact forces between the particles.

The rate form of the constitutive model only affects the internal force vector **I**. It has to be rewritten in a form suitable for the rate form of the constitutive model.

$$I_t = I_{t-dt} + d\,I_t \tag{36}$$

$$d\,I_t = \dot{I}_t\,dt = [\sum \int_{{}^1V} (\,B_\ell + B_{n\ell}\,)^T\ {}^2_1\dot{\sigma}\ \ d^1v + \sum \int_{{}^1V} \dot{B}^T_{n\ell}\ \ {}^2_1\sigma\ \ d^1v\ ]\,dt \tag{37}$$

At this point the rate form of the stress–strain relations can be introduced.

$${}^2_1\dot{\sigma} = C^{ep}\ {}^2_1\dot{\epsilon} - \dot{C}^t\,\dot{T} \tag{38}$$

The material property matrices will be described later. The introduction of Eq. 37 into Eq.38 leads to a expression for the rate of the internal force vector in terms of nonlinear stiffness matrices.

$$d\,I_t = (\,K_d + K_g\,)\,d({}^2U_t) - K_t\,dT_t \tag{39}$$

$$K_d = \sum \int_{{}^1V} (\,B_\ell + B_{n\ell}\,)^T\,C^{ep}\ \ (\,B_\ell + B_{n\ell}\,)\,d^1v \tag{40}$$

$$K_g = \sum \int_{{}^1V} G^T\,S\,G\,d^1v \tag{41}$$

$$K_d = \sum \int_{{}^1V} (\,B_\ell + B_{n\ell}\,)^T\,C^t\,\hat{N}\,d^1v \tag{42}$$

In this equation the K_d is the nonlinear displacement dependent stiffness matrix, K_g is the geometric stiffness which depends on the stress, K_t is the temperature stiffness matrix and **S** is stress dependent matrix.

The material property matrices result from the elasto–plastic constitutive model which will be described in a later section. At this point, we describe the generic form of these material property matrices.

$$ {}^{2}_{1}\dot{\sigma}_{ij} = C^{ep}_{ijkl}\ {}^{2}_{1}\dot{\epsilon} - C^{t}_{ij}\ \dot{\tau} \cdot \tag{43} $$

$$ C^{ep}_{ijkl} = C^{e}_{ijkl} - (C^{e}_{ijmn}\ n_{mn}\ n_{qp}\ C^{e}_{pqkl}\ )/(h + n_{nm}\ C^{e}_{mnpq}\ n_{qp}) \tag{44} $$

$$ C^{e}_{ijkl} = \lambda(\ \delta_{ij}\ \delta_{kl}\ ) + \mu(\ \delta_{ik}\ \delta_{jl} + \delta_{ik}\ \delta_{jl}\ ) \tag{45} $$

$$ C^{t}_{ij} = \theta\ (\ 3\lambda + 2\mu\ )\ \delta_{ij} \tag{46} $$

In this equation: λ and μ are the Lame constants; θ is the coefficient of thermal expansion; and C^{ep}_{ijkl} is the elasto−plastic stress−strain matrix. In Eq. (44) n_{ij} is the unit outward normal vector to the yield surface for the material model describing the behavior of the solid material in the particles, and h is the hardening parameter. The derivation of Eq. (44) is readily available in the relevant technical publications and will not be described here. The material model used in this study will be described in a later section.

$$ \boldsymbol{M}\ {}^{2}\ddot{\boldsymbol{U}}_{t} + (\boldsymbol{K}_{d} + \boldsymbol{K}_{g}\ )\ d({}^{2}\boldsymbol{U}_{t}\ ) - \boldsymbol{K}_{t}\ d\boldsymbol{T}_{t} = \boldsymbol{P}_{t} - \boldsymbol{I}_{t-dt} \tag{47} $$

The equation along with the thermal equation derived in the next section is integrated for each particle using the explicit integration method which will be described later.

3.2. Discrete Finite Element Thermal Energy Conservation Equation

The basic thermal energy conservation equation considered in this study includes the mechanical coupling effects.

$$ \nabla\ (k\ \nabla\tau) + c\ \dot{\tau} + \alpha\ \tau_{0}\ (3\lambda + 2\mu)\ \nabla^{T}\ \dot{u} + \beta\ \sigma^{T}\ \dot{\epsilon}^{p} = 0 \tag{48} $$

In this equation: k = the matrix of thermal conductivity; c = the thermal storage coefficient;

and, α and β are material parameters. The last term in Eq. (48) represents the inelastic dissipated energy.

The discrete finite element equation is determined from an integral functional whose Euler equation is Eq. (48). This functional is given in the following equation.

$$\int_v (\delta\nabla\tau)^T (k\ \nabla\tau)\ dv + \int_v \delta\tau\ c\ \dot{\tau}\ \ dv + \int_v \delta\tau\ \alpha\ \tau_0\ (3\lambda\ +\ 2\mu)\ \delta\tau\ \nabla^T \dot{u}\ dv$$

$$+ \int_v \beta\ \delta\tau\ \sigma^T \dot{\epsilon}\ dv - \int_A \delta\tau\ q_n\ da\ =\ 0 \tag{49}$$

In this functional the plastic strain has been replaced by the total strain. This is justified, since in the class of problems considered in this study the elastic strains are much smaller than the plastic strains.

The discretization of the temperature field within each finite element is given by Eq. (3). The gradient of the temperature is related to the nodal temperatures through an appropriate matrix B_τ.

$$\nabla\tau\ =\ \boldsymbol{B}_\tau\ T \tag{50}$$

$$\boldsymbol{B}_\tau\ =\ \begin{bmatrix} \boldsymbol{N}_{,\bar{x}} \\ \boldsymbol{N}_{,\bar{y}} \end{bmatrix} \tag{51}$$

The same matrix also relates the variation of the temperature gradient to the variation of the nodal temperatures.

$$\delta\nabla\tau\ =\ \boldsymbol{B}_\tau\ \delta T \tag{52}$$

Substitution of Eqs. (50), (52) into (49) results in the following discrete form of the integral equation.

$$\delta T^T \left(S \dot{T} + R \, {}^2\dot{U}_t + H T - Q \right) = 0 \tag{53}$$

$$S = \sum \int_{1V} c \, N^T N \, d^1v \tag{54}$$

$$R = \sum \int_{1V} \alpha \, \tau_0 \, (3\lambda + 2\mu) \, N^T \, \overline{G} \, d^1v + \sum \int_{1V} \beta \, N^T \, {}^2_1\sigma^T \, B \, d^1v \tag{55}$$

$$H = \sum \int_{1V} B_\tau^T \, k \, B_\tau \, d^1v \tag{56}$$

$$Q = \sum \int_{1A} N^T q_n \, d^1a \tag{57}$$

$$\overline{G} = \left[N_{,1\bar{x}} \; N_{,1\bar{y}} \right] \tag{58}$$

The discrete thermal equation is the direct consequence of the fact that Eq. (53) is valid for any arbitrary variation of the temperature δ**T** vector.

$$S \dot{T} + R \, {}^2\dot{U}_t + H T = Q \tag{59}$$

This equation along with the Eq. (47) is integrated for each particle using the explicit integration method which will be described in the next section.

4. Explicit Integration of Particle Discrete Finite Element Equations

The coupled discrete finite element equations for each particle given in Eqs. (47) and (59) are written in matrix form, suitable for the implicit integration methods. Some implicit integration methods are unconditionally stable, which would allow the use of reasonably large time steps. However, the implicit integration methods require the formation of matrices and solution of system equations for each particle. Consequently, the implicit methods were determined to be computationally too inefficient. Instead, it was decided to use an explicit method, which require rewriting the discrete equations in the following form.

$$\boldsymbol{M}\ {}^{2}\ddot{U}_t \ + \boldsymbol{D}\ {}^{2}\dot{U}_t \ = \boldsymbol{P}_t - \ \boldsymbol{I}_t \tag{60}$$

$$\boldsymbol{S}\ \dot{\boldsymbol{T}}_t \ = \ \boldsymbol{Q}_t \ + \ \overline{\boldsymbol{Q}_t} \tag{61}$$

$$\overline{Q} = \sum \int_{1V} \boldsymbol{B}_\tau^T \ \boldsymbol{q}\ d^1v + \sum \int_{1V} \alpha\ \tau_0\ (3\lambda \ + \ 2\mu)\ N^T\ \dot{\boldsymbol{\epsilon}}_v\ d^1v$$

$$+ \ \sum \int_{1V} \beta\ N^T\ ({}^{2}_{1}\boldsymbol{\sigma}^T\ \dot{\boldsymbol{\epsilon}})\ d^1v \tag{62}$$

$$\boldsymbol{q} \ = \ \boldsymbol{k}\ \boldsymbol{B}_\tau\ \boldsymbol{T} \tag{63}$$

$$\dot{\boldsymbol{\epsilon}}_v \ = \ \nabla^T \dot{u} \tag{64}$$

A global damping term, represented by the matrix **D**, is introduced to model a global energy dissipation in the material. As a numerical convenience, **D** is assumed to be proportional to the mass matrix, $\mathbf{D} = \gamma\ \mathbf{M}$.

A finite time step Δt is used to discretize time and the standard central difference method is used.

$$ {}^2\ddot{U}_t = ({}^2\dot{U}_{t+\frac{1}{2}\Delta t} - {}^2\dot{U}_{t-\frac{1}{2}\Delta t})/\Delta t \tag{65} $$

$$ {}^2\dot{U}_t = ({}^2\dot{U}_{t+\frac{1}{2}\Delta t} + {}^2\dot{U}_{t-\frac{1}{2}\Delta t})/ 2 \tag{66} $$

$$ \dot{T}_t = (\dot{T}_{t+\frac{1}{2}\Delta t} + \dot{T}_{t-\frac{1}{2}\Delta t})/ 2 \tag{67} $$

Substitution of Eqs. (65) and (66) into Eqs. (60) leads to the following equation for the velocity vector. Similarly, substitution of Eq.(67) into Eq. (61) leads to the vector of the temperature rate. These vectors are then used to update the displacements and temperatures vectors .

$$ {}^2\dot{U}_{t+\frac{1}{2}\Delta t} = c_1 \, {}^2\dot{U}_{t-\frac{1}{2}\Delta t} + c_2 \, M^{-1} (P_t - I_t) \tag{68} $$

$$ \dot{T}_{t+\frac{1}{2}\Delta t} = \dot{T}_{t-\frac{1}{2}\Delta t} + 2 \, S^{-1} (Q_t + \overline{Q_t}) \tag{69} $$

$$ c_1 = \frac{2-\gamma \, \Delta t}{2 + \gamma \, \Delta t} \tag{70} $$

$$ c_2 = \frac{2 \, \Delta t}{2 + \gamma \, \Delta t} \tag{71} $$

$$ {}^2U_{t+\Delta t} = {}^2U_t + \Delta t \; {}^2\dot{U}_{t+\frac{1}{2}\Delta t} \tag{72} $$

$$ T_{t+\Delta t} = T_t + \Delta t \; \dot{T}_{t+\frac{1}{2}\Delta t} \tag{73} $$

In Eqs. (68) and (69) the inverses of the matrices **M** and **S** are needed. A diagonal form of these matrices are used to avoid solution of system of equation. It is commonly understood that diagonalizing these matrices has very little influence on the results.

The explicit second central difference method is conditionally stable. The method is stable for time all steps less than a critical time step Δt_{cr}. Theoretically, the critical time step

is related to the highest natural frequency of the system by the following well known stability criterion.

$$\Delta t \leq \Delta t_{cr} \tag{74}$$

$$\Delta t_{cr} = \frac{2}{\omega_{max}} \tag{75}$$

The maximum natural frequency of the system, ω_{max}, is related to the smallest finite element in the smallest particle. However, in discrete finite element method much smaller time steps are needed. This is mainly due to the fact that the collision of particles at high velocities produce apparent cycles of contact and debonding, with apparent periods much smaller than the smallest natural period of the system. Our experience has been that the critical stable time step for discrete finite element method is usually one hundredth to one thousandth of the natural frequency based critical time step in Eq. (75), depending on the maximum particle velocities.

5. Contact Model

The particles are modelled by individual finite element meshes. The particles can undergo large displacements and large rotations, as well as large deformations. The interaction between particles is modelled through contacts between adjacent particles. Contact between two particles is assumed to occur when the boundary regions of the particles overlap, as shown in Fig 4. Also shown in Figure 4 is the contact between two elements, one from each particle. The overlap occurs over a portion of the edges of the elements in contact. The main tasks are: (1) detection of the contacts; (2) determination of normal and shear relative displacements at the contacts; and, (3) determination of the contact forces from the contact relative displacements.

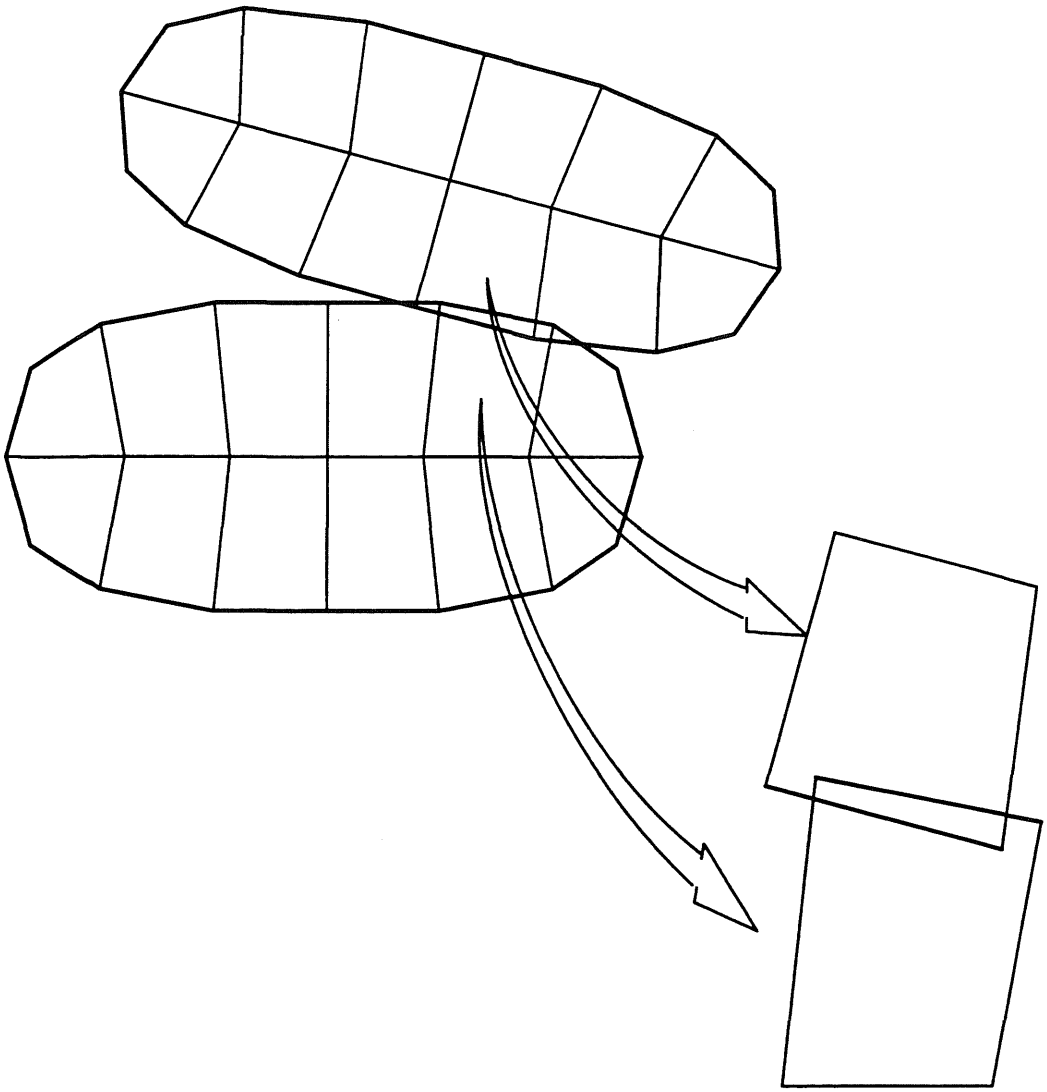

Figure 4. Contact between two particles and their two finite elements

Contact detection is the most time consuming part of the analysis. It often takes more than 80% of the total computational time in Discrete Finite Element analysis. The procedure for contact detection has been described in some of the previous publications (1 through 10). In order to limit the number of checks, the total region of the analysis is divided into smaller subregions by a rectangular equidistant mesh. A running record of the position of each particle and its elements in reference to these subregion is kept and frequently updated. Contact detection is performed by checking each side of each element with respect to the sides of all elements

within its subregion and its surrounding subregions. The detection is done at two levels. First, a quick check identifies particles and elements which are likely to be in contact. This initial check eliminates the particles and elements which are too distant and reduces the total number of computationally costly contact checks. The second level of contact detection performs a more thorough check for those particles and elements which were identified as likely to be in contact

Once a contact has been identified between two elements the next step is to determine the normal and shear relative displacements at the contact. As shown in Figure 5, the contact relative displacements are determined from the actual overlap between the two elements, which can be divided into a normal component and a shear component. The contact forces are determined from the contact relative displacements by using the contact constitutive model. These contact forces are assumed to act along a line bisecting the overlap area between the two elements in contact.

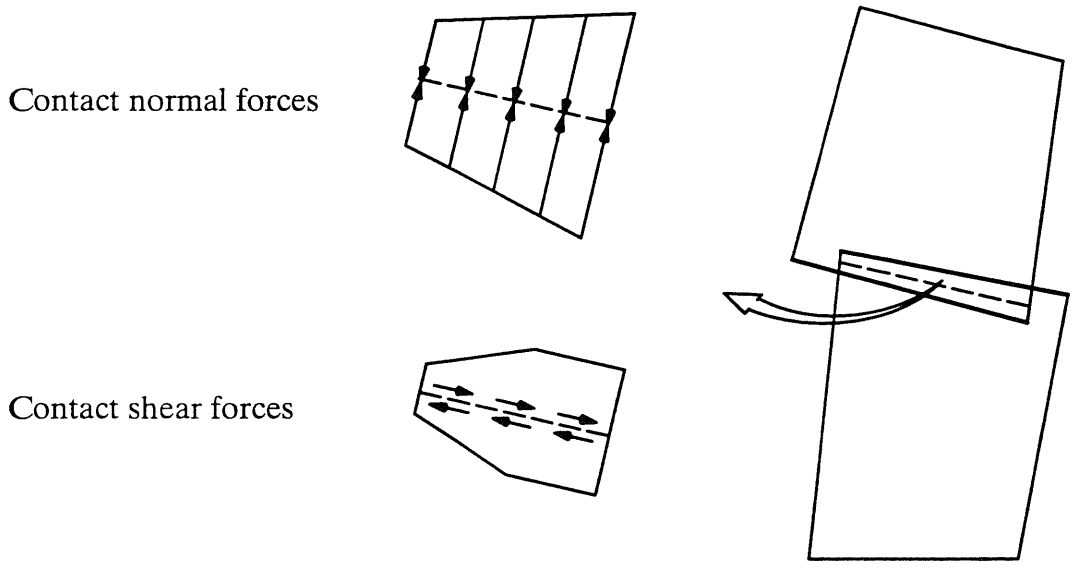

Figure 5. Contact relative displacements and normal and shear forces.

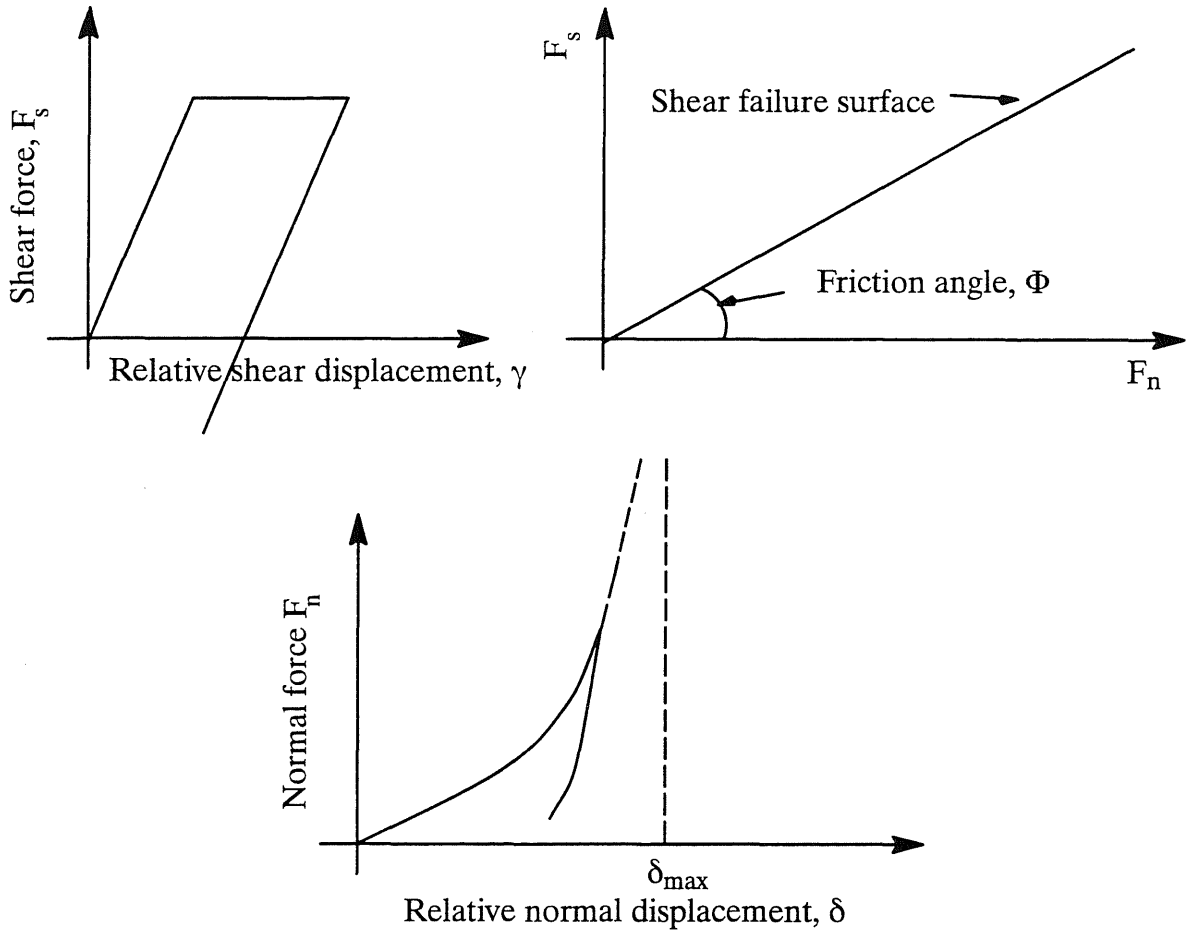

Figure 6. Contact constitutive model.

The constitutive behavior at the contacts is represented by a friction based model along with a nonlinear normal force–normal relative displacement relationship. The contacts are assumed to be incapable of sustaining tension, such that any tensile normal relative displacement will cause debonding and separation. In compression, the normal force–normal relative displacement relationship is a hardening type, as shown in Figure 6. The normal stiffness starts with an initial value and asymptotically approaches infinity at a maximum value of the normal relative displacement. In shear, the constitutive behavior is elastic–perfectly plastic. The maximum contact shear force is assume to be a linear function of the normal contact force, as shown in Figure 6.

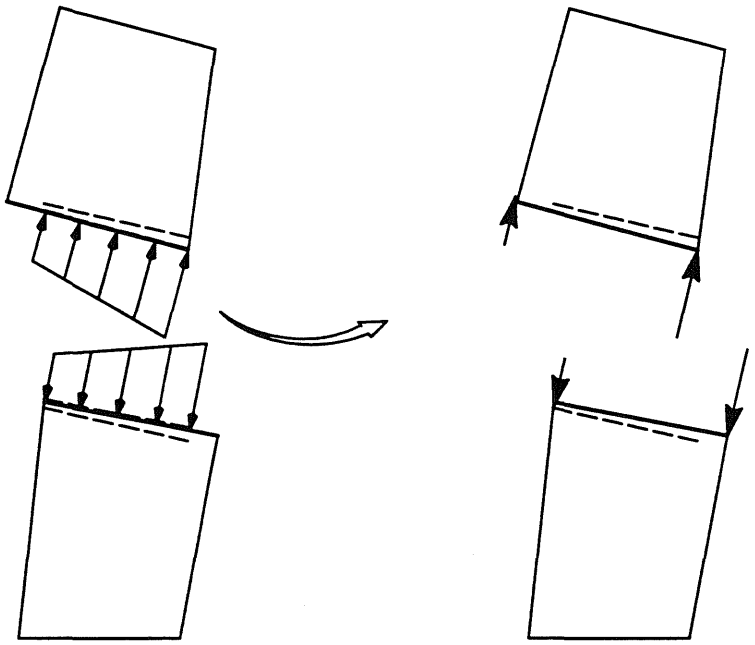

(a) Transformation of normal forces

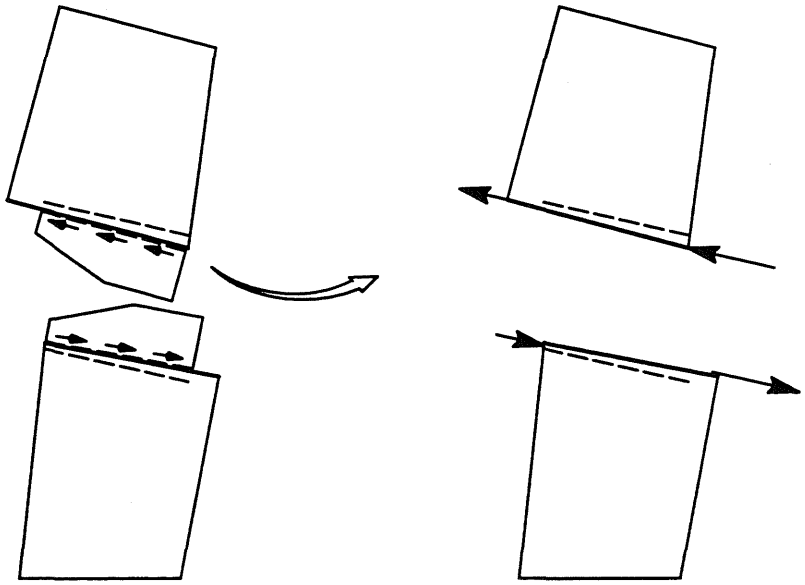

(b) Transformation of shear forces

Figure 7. Transformation of the contact forces to equivalent nodal forces.

The distributed forces can not be directly used in the analysis. They must first be transformed to equivalent nodal forces, as shown in Figure 7. The distributed contact forces are transformed to the equivalent nodal forces by using the second half of Eq. (35). These nodal displacements are then transformed to global coordinate system and used in the analysis.

6. Constitutive Material Behavior

The constitutive behavior of solids have been modelled with a plasticity model. It is assumed that the material behavior of the solid particles resemble the behavior of geomaterials, for which an extensive body of research literature is available. We have specially chosen the Cap model which was originally developed by Sandler and Dimaggio (12). This model was selected because it was specially developed for the study of weapons effects which involved the material behavior under very high pressures, similar to the conditions in the class of problems considered this study. Geomaterials generally have very small tensile strength and their behavior in compression is be characterized under two different stress paths. When subjected to increasing shear or deviatoric stresses, the material yields and produces permanent plastic strains. Under increasing isotropic stress (pressure), the material exhibits a typical Hugoniot type pressure−volumetric strain relationship. The effective bulk modulus of the material asymptotically approaches very high values at high pressures, with asymptote located at the maximum value of the plastic volumetric strain. The material hysteresis occurs both under cyclic deviatoric stresses and the cyclic volumetric stresses. However, the largest portion of the dissipated inelastic energy, which acts as a thermal source, is generated under cyclic deviatoric strains.

Cap Plasticity Model Cap model used in this study is similar to the model proposed by Sandler and Rubin (1979). It consists of a perfectly plastic failure surface, f_1 , which is defined in terms of the first and second invariants of stress through the following equation.

$$f_1 = \sqrt{J} - [\, A - C \exp{(BI)} \,] = 0 \tag{76}$$

The shear strength in this models increases with the mean stress, similar to most frictional materials. However, this increase is less than linear. A simpler linear relationship between the

shear strength and the mean stress is often used in problems where the stresses remain relatively low. Furthermore, as shown in Figure 8 in tension, the yield surface has a vertical cut−off.

The cap part of the material model is represented by a strain hardening surface, f_2 , described by the following equations.

$$f_2 = \sqrt{J} - (1/R) \{ [X(k) - L(k)]^2 - [\sqrt{J} - L(k)]^2 \}^{1/2} = 0 \quad (77)$$

$$k = f(\epsilon^p) \quad (78)$$

$$X(k) = -1/D \; ln(1 - k/W) \quad (79)$$

The cap is a hardening yield surface. It moves outward as a function of the volumetric compressive plastic strain.

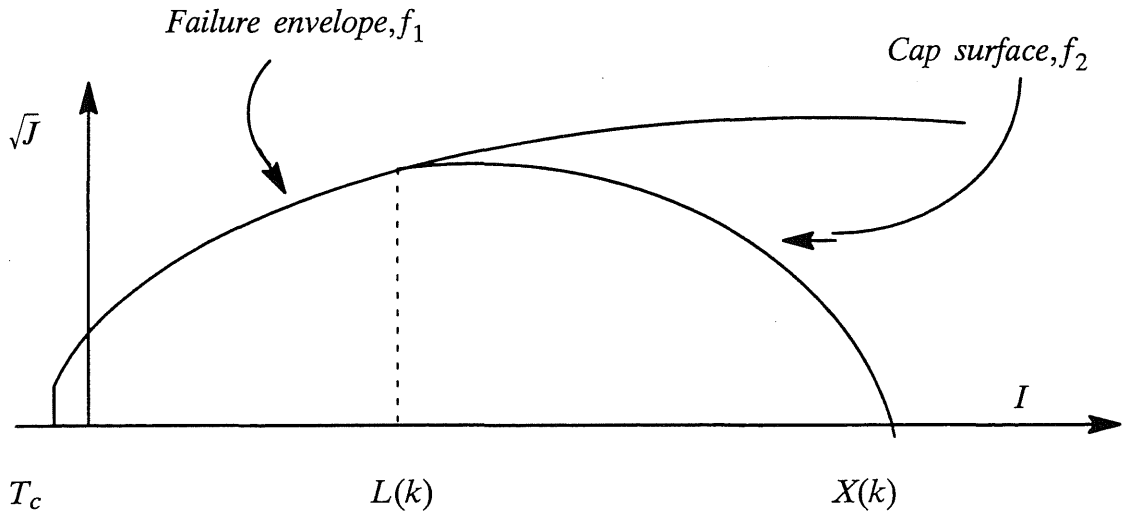

Figure 8 Cap Model for constitutive behavior of geo−materials

In these equations I and J are the first and the second stress invariants, A , B , C , D , and R are material properties. Also k is a parameter that can be a complicated function

of the first invariant of plastic strain ϵ^p and W is the maximum possible plastic volumetric strain of the material.

Associated flow rule is used with both the failure surface and the cap. When the stress point reaches each surface, the plastic strain increment is assumed to be normal to the yield surface at that point.. The hardening rule associated with the failure surface is perfectly plasticity, while the material Hugoniot provides the hardening rule for the cap.

7. Validation Case Study

As an illustrative example and a validation case study, we have applied the DFEM, described in the previous sections to model and analyze one of the experiments reported by Sheffield et al. in Ref. (14). This analysis was performed in isothermal condition. Part of the experimental setup considered in the analysis is shown in Figure 9. In this experiment a 4 mm thick specimen of HMX is confined in a chamber and it is subjected to an impact by a hammer travelling at the velocity V_0. The impact generates a shock wave, which travels through the granular material and compacts it. In this analysis we have modelled a portion of the specimen, sufficiently away from the lateral boundaries, with DFEM, as shown in Figure 9. Only the inert condition has been modelled, since the DFEM developed so far does not include the chemical reaction effects to model the deflagration and detonation phases. The analysis is done in two phases. First, the initial condition shown in Figure 9 is generated by a process of deposition, then the DFEM model is subjected to impact.

7.1. Generation of Initial Condition

Grains are modelled as elliptic particles. The dimensions of the particles are randomly varied over a specified range. Each particle is modelled with a finite element mesh of six elements. The hammer and the bottom of the chamber have also been modelled, each with three elements. The initial condition and the initial arrangement of the particles in the specimen

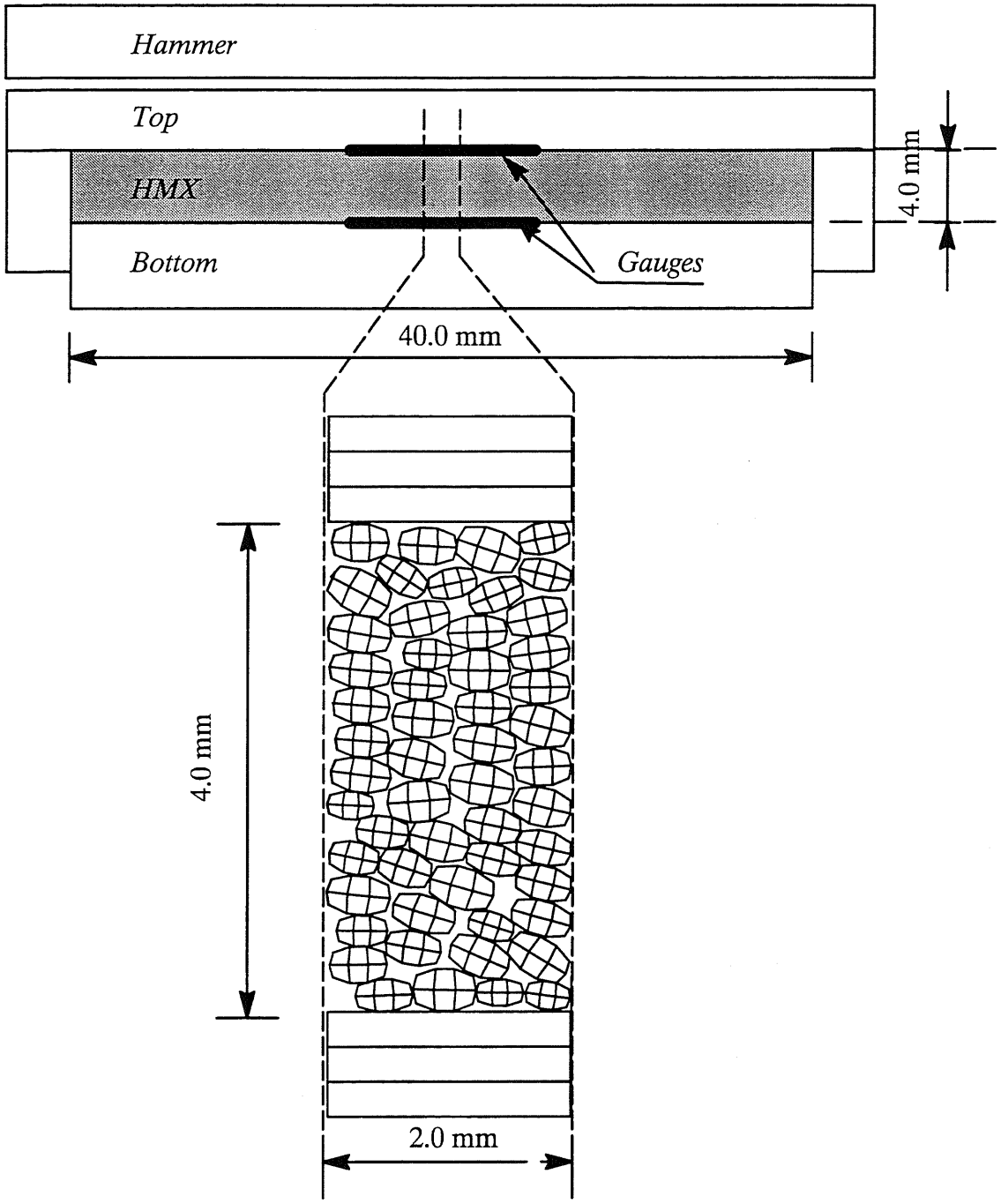

Figure 9. Experimental setup and a portion of the specimen and its DFEM model.

are in reality a result of a specific process. This process may include one or more of the following: slow deposition; pouring from a height; raining from a height; compaction; and, vibration. The method of preparation of the sample has an important effect on its composition, properties and its subsequent behavior. For example, the behavior of energetic materials are thought

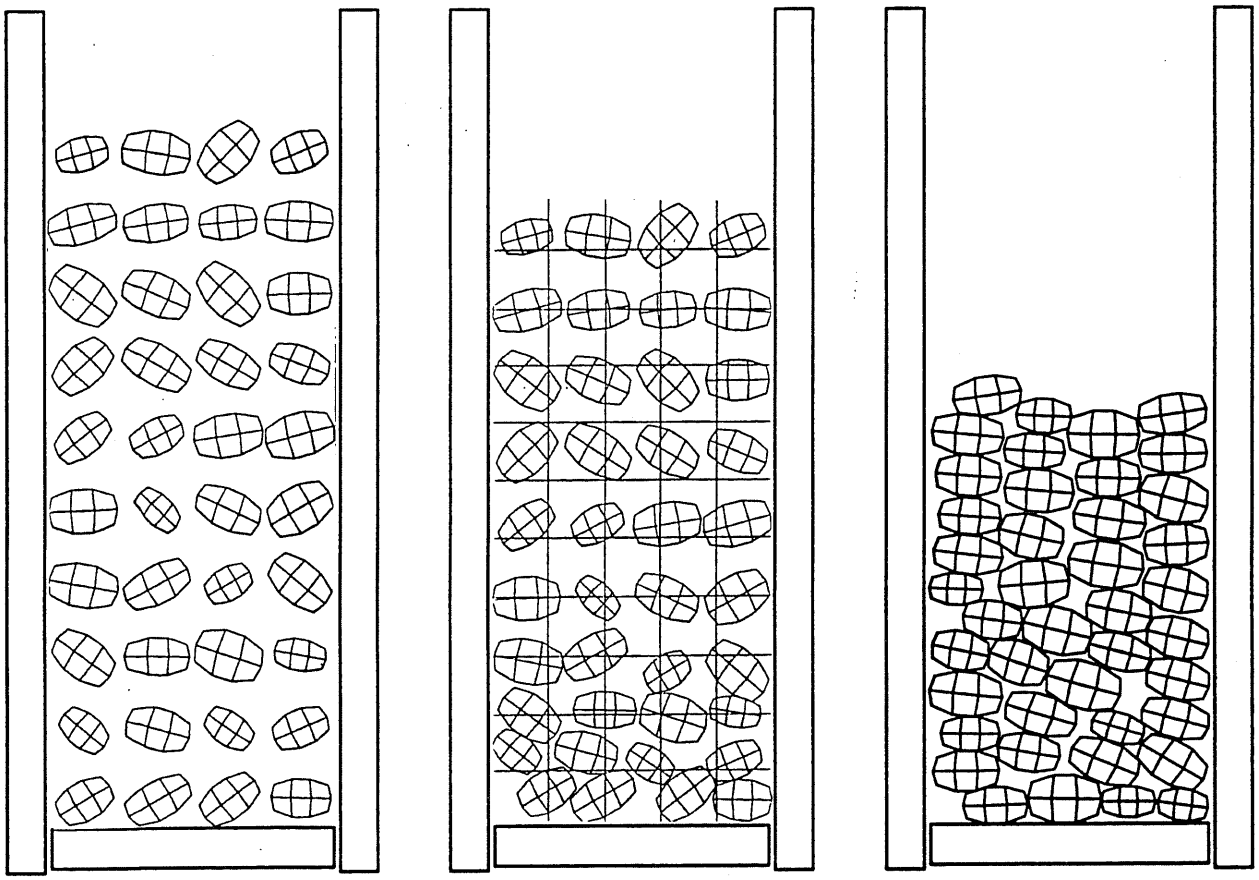

Figure 10. The process of the generation of the initial condition.

to be influenced by their initial porosity and density which is influenced by the method of sample preparation. In order to obtain as realistic an initial condition as possible, the method of sample preparation must be simulated as closely as possible. In this study, we have simulated the process of sample preparation, first by raining the particles into a container, as shown in Figure 10, until the container is filled. Then, a heavy weight was dropped on the sample to compact it further. During this process a very high contact stiffness was used to keep the particles as separate as possible. The analysis was continued until the particles and the surcharge weight reached equilibrium. The final state of the simulation of the sample preparation is the state of the particle assembly shown in Figure 9, and it formed the initial condition in the dynamic phase of the analysis.

7.2. Analysis of Shock Compression

In this phase, the grains, the hammer and the bottom of the chamber have been modelled as elasto−plastic materials represented by the Cap model described earlier. The material properties were identified through a procedure of trial and error so as to obtain a material Hugoniot in the analysis, as close to the experimentally observed Hugoniot of HMX as possible. The experiment simulated in this study is the shot 912 of the series of experiments performed at the Los Alamos National Laboratory (14). The material used in this experiment is coarse grain HMX with a density of $\varrho = 1.24\ gr/cm.$ The initial hammer velocity in the experiment was $V_0 = 288$ m/sec.

As can be seen in Figures 11, 12 and 13, the impact of the hammer generates a compression wave, which propagates through the granular material and compresses it. The wave front is clearly visible in Figure 11. The wave front reaches the bottom of the chamber in approximately 8 μsec. The average velocity of the compression wave front is about 500 m/sec, which is almost twice the initial velocity of the hammer.

The wave front propagates approximately along a line, with some minor deviations. This is probably due to the fact that only four particles have been modelled across the specimen and the lateral boundaries are assumed to be frictionless so that the model can represent the fact that only a small part of the actual specimen is being analyzed. In the vicinity of the lateral boundaries of the actual specimen, the friction may affect the shape of the wave front.

Figures 12 shows the comparison of the calculated and measured time histories of the velocity and stress. In the experiment, the measurements are made by two sets of velocity and stress gauges, one set located at the interface between the hammer and the specimen and the second set located at the interface between the specimen and the bottom of the chamber. The actual gauges are in contact with many particles. They measure average quantities over regions containing many particles. The dashed lines in Figures 12 are approximate measurement, which have been reproduce from the results reported in Ref. (14). The calculated valued

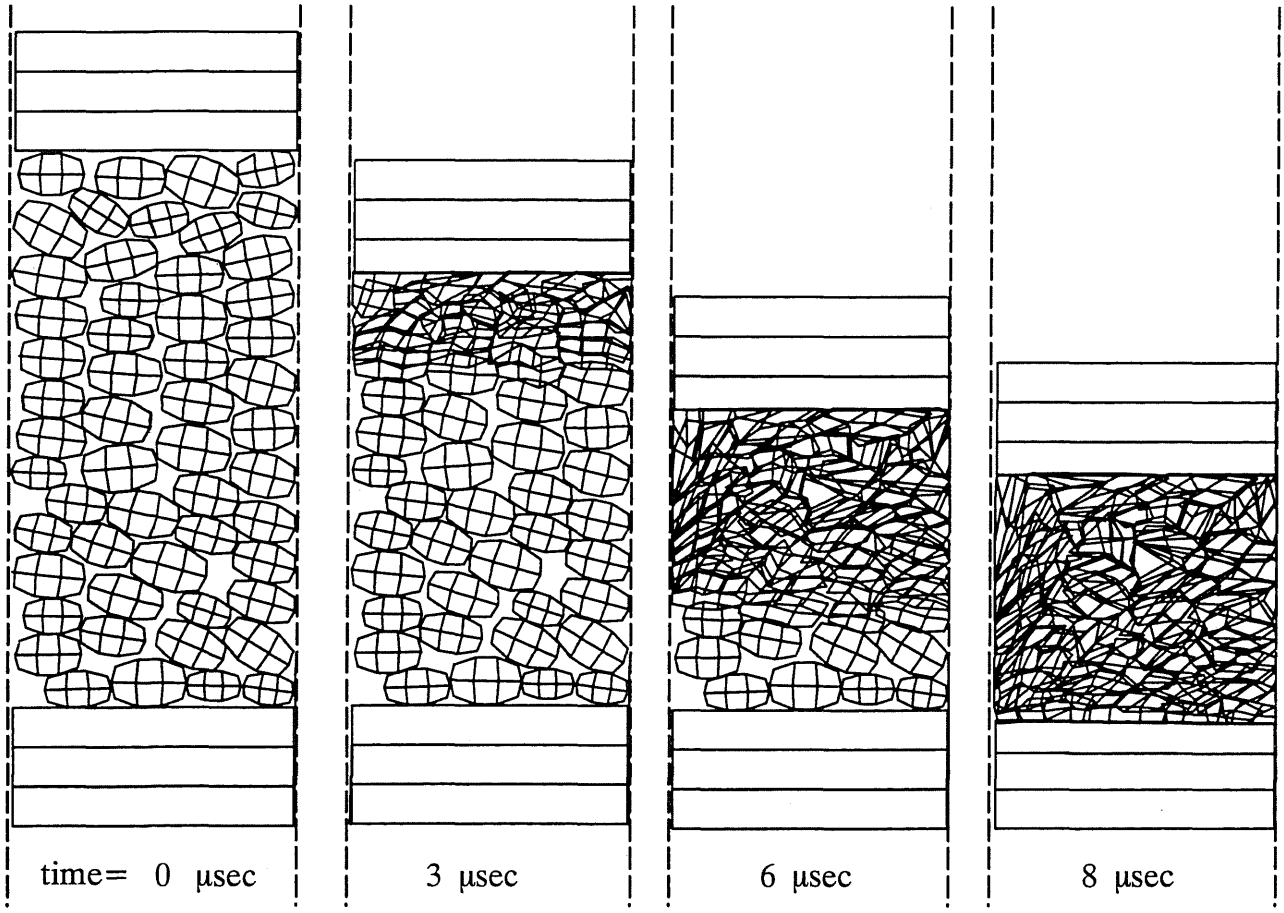

Figure 11. Propagation of the shock front and compression of the granular media.

are taken from the lowest element of the hammer and the top element of the bottom of the chamber. The local effects, causing oscillations are more pronounced in the calculations, since they represent the averaged quantities only over four particles. The results of the analysis are qualitatively similar to the experimental observations, except for a difference of 2.0 μsec in the arrival time. This difference is very likely due to the assumed values of the material properties, in absence of more accurate measured data. Also, it is anticipated that the actual modelling of the gauges would improve the accuracy of the results of analysis. Another factor contributing to the discrepancy between the measurement and analysis is the fact that isothermal conditions were used in the analysis. It is interesting to note that the lower gauges, at the bottom of the chamber exhibit a much slower rise time than those at the gauges at the top of the speci-

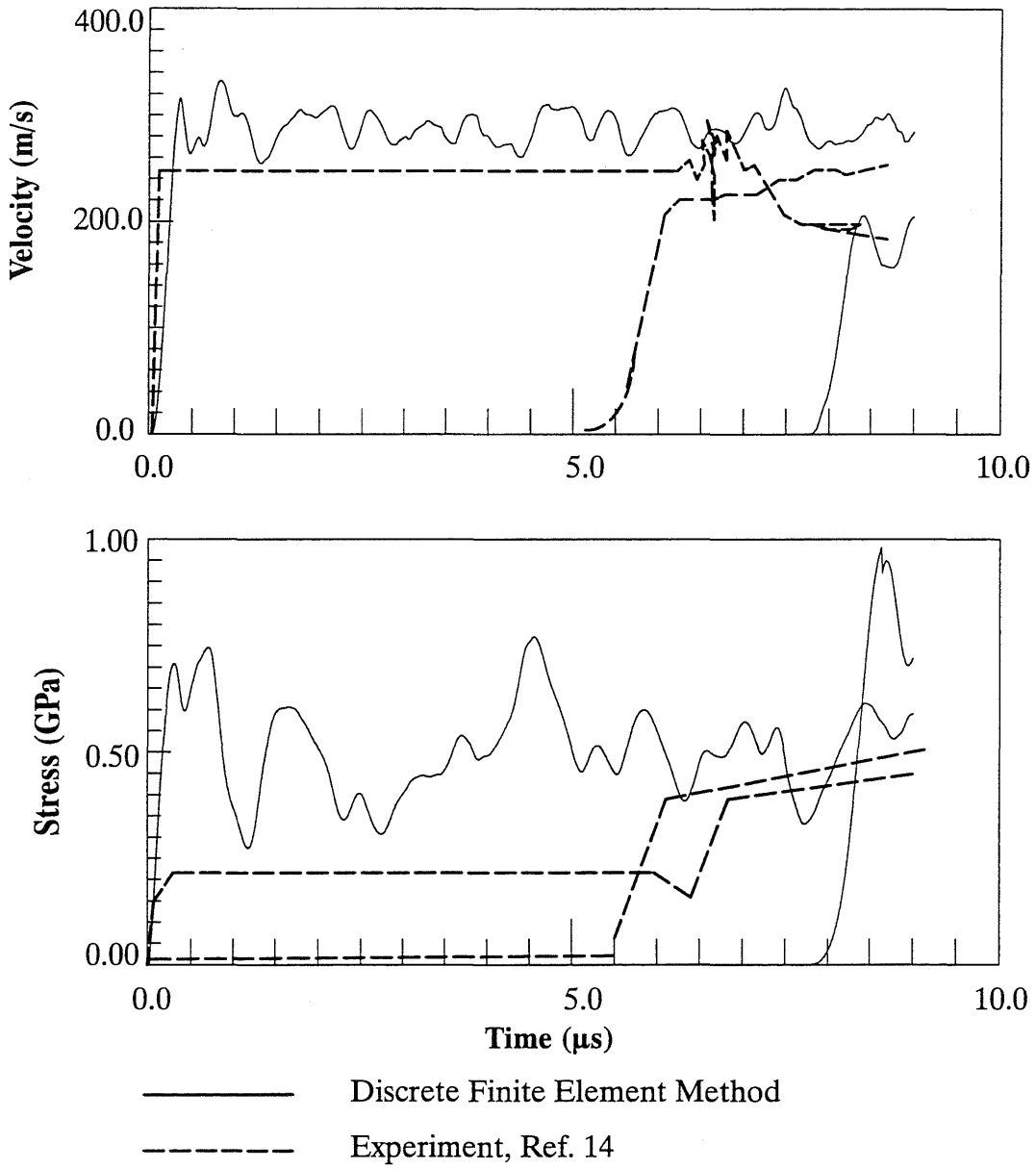

Figure 12. Comparison of the measured and computed velocity and stress time histories.

men, at the point of impact. This is, no doubt, the result of the dispersive waves which have developed during the propagation of the wave front through the sample. The effect is clearly observed in the results of the analysis which show a remarkable similarity with the measurements. The dispersion in the analysis is due to the granularity and the inelasticity of the material.

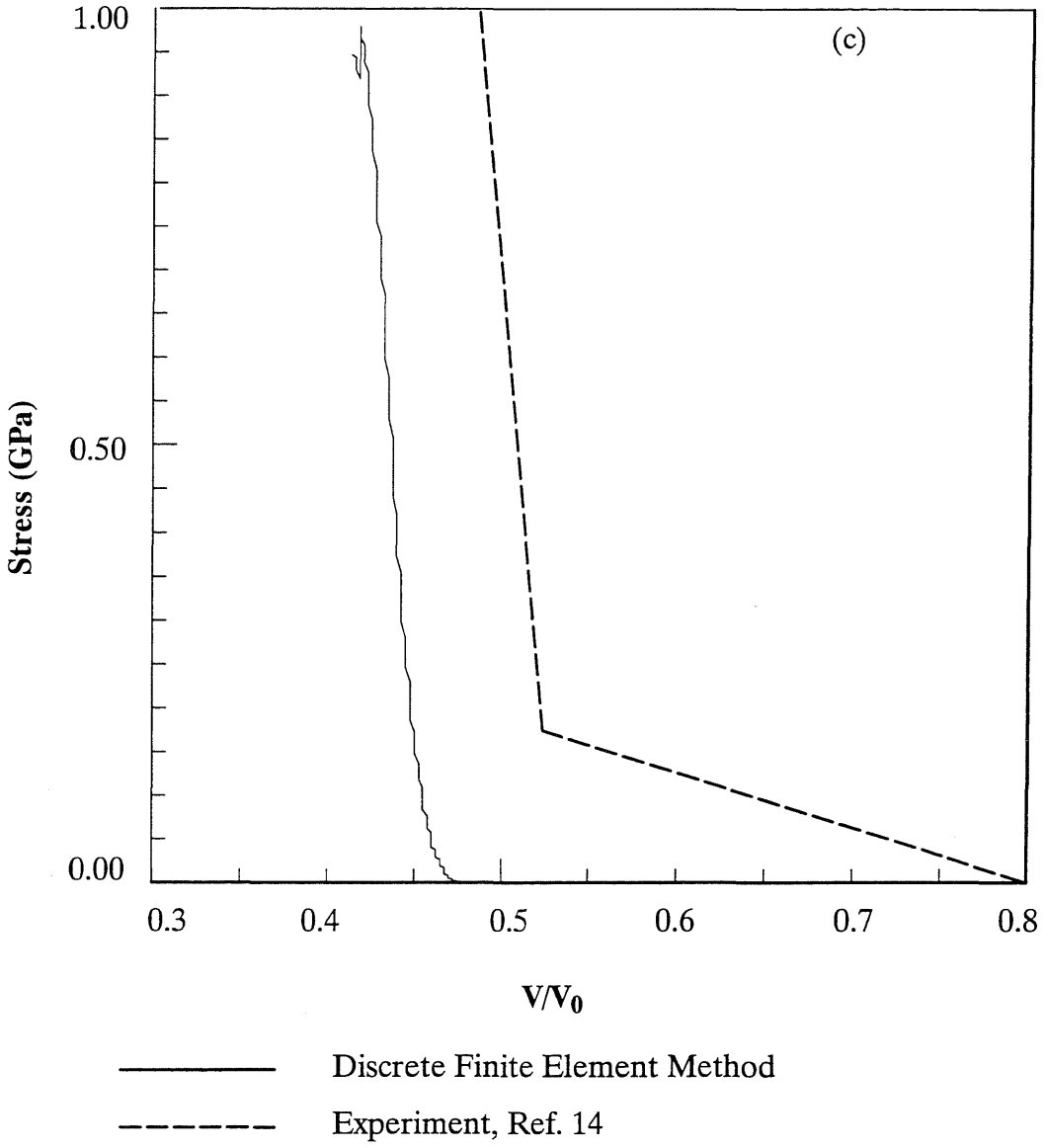

Figure 13. Comparison of the measured and computed Hugoniot.

Figure 13 shows the experimental and calculated Hugoniot of the granular material. The dashed line has been approximately reproduced from the data taken from the Ref. 14. The solid line is the calculated value for the whole specimen. Again, the results are qualitatively similar. This aspects of the analysis results are quite sensitive to the assumed hardening parameters for the cap model. In absence of hard data, some reasonable value were assigned to the hardening parameters. More accurate data, would improve the results of the analysis.

8. Concluding Remarks

A new methodology has been developed in this study for the dynamic thermo–mechanical analysis of deformable granular materials, using the Discrete Finite Element Method, which was originally developed by Ghaboussi and his co–workers. The method allows modelling of the particles with individual finite element meshes. These particles are allowed to undergo large displacements, rotation and deformations. Cap plasticity model was used to represent the constitutive behavior of the solid particles. The motion and deformation of the particles were modelled using the Updated Lagrangian method, coupled with a discrete thermal diffusion equation. The contact between the particles were modelled with a friction based nonlinear material model. A computer program DFEM2000 was developed and used in the analysis of a validation case study. An experiment performed at the Los Alamos National Laboratory was simulated. The results of the analysis compare well, qualitatively, with the experimental results.

This study is a good first step in modelling and analysis of the behavior of the energetic materials. By closely modelling the granular structure of the material and its micro–mechanical fabric, it has the potential of enabling the study of the effect of parameters, such as porosity and density, which can not be easily studied with the continuum models. With further development of this methodology and by inclusion of chemical reaction effects, it would be possible to study and gain insights into the micro–mechanics of the process of shock compression, deflagration and detonation.

Further development of the methodology should include extension of the program to include; breakage and crushing of the particles; more realistic material models based on hard data; chemical reaction effects including deflagration and detonation; modeling of the effect of voids and pores; and, a thorough parametric study to determine the sensitivity to material parameters, method of sample preparation and initial porosity and density. Long term developments may include extensions to three dimensions.

9. References

1. Barbosa R. and J. Ghaboussi. (1988) "Discrete Element Model for Granular Soils," *Proceedings, Workshop on Fill Retention Structures*, Ottawa, Canada.
2. Barbosa R. and J. Ghaboussi. (1989) "Discrete Finite Element Method," *Proceedings, First International Conference on Discrete Element Method*, Denver, Colorado,.
3. Barbosa R. and Ghaboussi J., (1990),'Discrete Finite Element Method for Multiple Deformable Bodies', Finite Elements in Analysis and Design, v.7, 145–158.
4. Barbosa R. and J. Ghaboussi (1990) "Discrete Finite Element Method for Multiple Deformable Bodies", *Journal of Finite Elements in Analysis and Design*, Vol. 7, Oct., pp 145 – 158
5. Barbosa R. and J. Ghaboussi. (1992) "Discrete Finite Element Method," *Engineering Computations*, Vol. 9, June, pp 253–266.
6. Ghaboussi, J. (1989) "Fully Deformable Discrete Element Analysis Using a Finite Element Approach," *International Journal of Computers and Geotechnics*.
7. Ghaboussi, J. and R. Barbosa. (1988) "Water Pressure Effects in Jointed Rock with Deformable Bodies," *Proceedings, ASCE/EMD Specialty Conference: Mechanics of Media with Discontinuities*, Blacksburg, Virginia.
8. Ghaboussi, J. and R. Barbosa. (1990) "Three–Dimensional Discrete Element Method for Granular Materials," *International Journal for Numerical and Analytical Methods in Geomechanics*, vol. 14, pp 451–472..
9. Ghaboussi, J., (1992) "Some Theoretical and Computational Aspects of Large Scale Discrete Element Analysis," *Proceedings, 33rd U.S. Symposium on Rock Mechanics*, Santa Fe, New Mexico.
10. Ghaboussi, J., M. Basole and S Ranjithan (1993) "Three–Dimensional Discrete Element Analysis on Massively Parallel Computers", Proceedings, Second International Conference on Discrete Element Methods, MIT.
11. Joghataie, A. and J. Ghaboussi, (1996) "Shock Compression in Granular Media Using Discrete Finite Element Method", *Proceedings, 11th ASCE Engineering Mechanics Conference*, Ft. Lauderdale.
12. Sandler I.S., DiMaggio F. L. and Baladi G.Y., (1976), 'Generalized Cap Model for Geological Materials', *J. Geotechnical Engineering, ASCE*, v.102, n.GT7, 683–699.
13. Sandler I. S. and Rubin D., (1979), 'An Algorithm and A Modular Subroutine For the Cap Model', *Int. J. for Numerical and Analytical Methods in Geomech.*, v.3, 173–186.
14. Sheffield S. A., Gustavsen R. L. and Alcon R. R., (1993), 'Shock Initiation Studies of Low Density HMX Using Electromagnetic Particle Velocity and PVDF Stress Gauges', *Tenth International Detonation Symposium, Boston, MA*, July 12–16.